# The hydraulic conductivity of a shaped fracture with permeable walls*

Daihui Lu[a], Federico Municchi[b] and Ivan C. Christov[a,*,1]

[a]School of Mechanical Engineering, Purdue University, West Lafayette, Indiana 47907, USA
[b]School of Mathematical Sciences, University of Nottingham, University Park, Nottingham, NG7 2RD, UK

ARTICLE INFO

*Keywords*:
hydraulic conductivity
wall permeation
rock fracture
lubrication flow

ABSTRACT

We investigate the flow-wise variation of the hydraulic conductivity inside a non-uniformly shaped fracture with permeable walls. Using lubrication theory for viscous flows, in conjunction with the Beavers–Joseph–Saffman boundary condition at the permeable walls, we obtain an analytical expression for the velocity profile, conductivity, and wall permeation velocity. These predictions highlight the effects of geometric variation (through the local slope of the aperture's flow-wise variation), the permeability of the walls (through a dimensionless slip coefficient), and the effect of flow inertia (through a Reynolds number). The theory is validated against an OpenFOAM® solver for the Navier–Stokes equations subject to a tensorial slip boundary condition, showing good agreement. The mathematical results have implications on system-level (multiscale) modeling of hydraulically fractured reservoirs, in which the Darcy conductivity of each non-uniform passage must be accurately accounted for, throughout the fractured porous rock.

## 1. Introduction

Crude oil and natural gas exist as fluids in large underground reservoirs in sedimentary basins around the world. They occupy the connected porous media within strata of sedimentary rocks, typically sandstones or carbonates [18]. Over the last decade, hydraulic fracturing ("fracking") of shales has paved the way towards increasing the recoverable reserves of oil and gas in the United States [32]. During fracking, complex fluids (primarily water-based suspensions with dispersed particulates termed "proppants") [64, 4] are pumped into tight formations [15, 41]. Fracking is inherently a multiscale problem [23]: as the injected high-pressure fluid enters a rock formation from the well bore, a complex array of cracks of various shapes, sizes, and with flow-wise variations, are created [64, 46]. This network of fractures increases the conductivity of the rock formation by increasing the available flow area [43, 60]. Similarly, in enhanced geothermal systems [34], heat is extracted from hot rocks by flooding the dry fracture network [35, 40]. Thus, it is of practical importance, as well as of fundamental scientific interest, to create mathematical models of the conductivity in complex and non-uniform fractures. In this letter, we derive a novel mathematical expression for the conductivity of a shaped fracture with flow-wise geometric variations.

To provide a sense of the scale on which the half-aperture $h$ of a fracture may vary with the flow-wise direction $x$, consider the standard Perkins–Kern–Nordgren (PKN) and the Khristianovitch–Zheltov–Geertsma–de Klerk (KGD) models, which idealize fractures as long and narrow elliptical cracks [45]. Garagash and Detournay [17] showed that the fracture tip has a shape with $h(x) \sim (x_{\text{tip}} - x)^{1/2}$ as $x \to x_{\text{tip}} > L$. (The typical fracture geometry we consider has total length $L_{\text{total}}$, appreciable variations in the shape occur over some typical scale $L \ll L_{\text{total}}$, with the tip falling outside the domain in Fig. 1.) Thus, the shape gradient away from the crack tip goes as $\alpha = dh/dx \sim -(x_{\text{tip}} - x)^{-1/2}$. Clearly, as $x \to -\infty$ (away from the crack tip), $|\alpha| \to 0^-$, justifying the small slope assumption $|\alpha| \ll 1$. Typical fracture geometry parameter values are summarized in Table 1, further justifying that, away from the crack tip, $dh/dx \sim |\alpha| \ll \epsilon = h_0/L$; that is, the fracture's typical slope is much smaller than its aspect ratio. (Although our analysis does not depend on the sign of $\alpha$, we henceforth take $\alpha < 0$ for definiteness.)

The simplest model of fracture conductivity (the parallel-plate model [66]) assumes that fracture walls are smooth, impermeable walls with a *constant* aperture of $2h_0$ (distance between the walls) and span $w$ (length in the transverse direction); see Fig. 1. By analogy to lubricating viscous flow between two plates (the so-called Hele-Shaw model [5]), one can calculate the hydraulic conductivity to be $\mathcal{K} = h_0^2/3$. Then, the transmissivity of the fracture ($\propto h_0 w \mathcal{K}$) follows the well-known "cubic law" [63]. However, the flow passages in both naturally [18] and hydraulically fractured [64] formations have a *variable* aperture $2h(x)$. Generally, the walls of fractures are not parallel [13], in part due to the flow-wise deformation of the fracture due to large injection pressures [24], requiring corrections to Darcy's laws arise via a modified conductivity and transmissivity models [26, 61, 48]. However, these models are for *impermeable walls*.

The bounding surfaces of a fracture are the porous rock formations themselves, therefore they should not be idealized as impermeable plates [8]. Permeation of gas into the matrix, and its subsequent diffusion, affects the late-years productivity of fractured wells [42, 27]. Berman [9] and Sellars [51] investigated the effects of a permeable wall in a

*Acknowledgment is made to the donors of the American Chemical Society Petroleum Research Fund for support of this research under ACS PRF award # 57371-DNI9.

*Corresponding author
christov@purdue.edu ( Ivan C. Christov)
tmnt-lab.org ( Ivan C. Christov)
ORCID(s): 0000-0001-9837-2774 ( Daihui Lu); 0000-0002-5105-6173 ( Federico Municchi); 0000-0001-8531-0531 ( Ivan C. Christov)
[1]Also affiliated with the Center for the Environment at Purdue University.

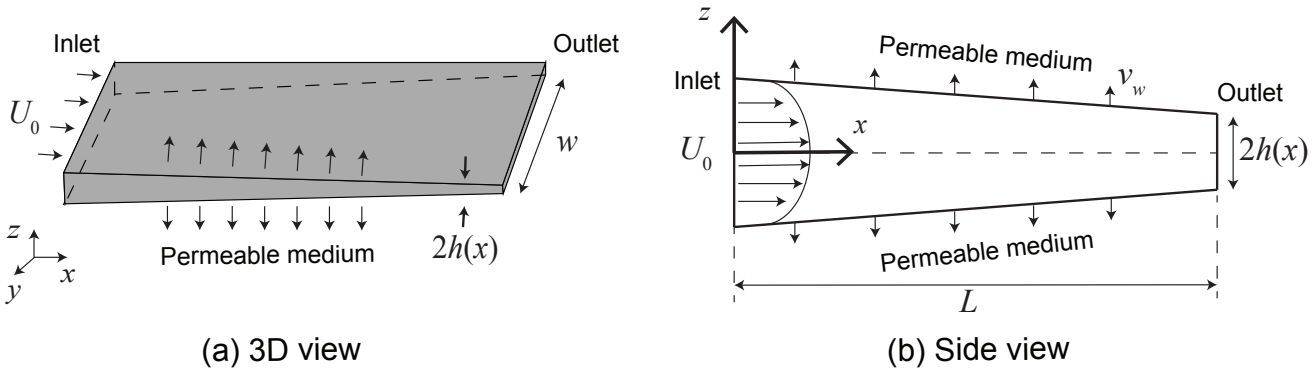


**Figure 1:** Schematic of a typical fracture flow geometry idealized as a Hele-Shaw cell. The fracture's shape varies appreciably over a "typical" length $L$, and it has a constant gradient $dh/dx \sim \alpha$, so that the half-aperture is $h(x) = h_0 + \alpha x$ (to a linear approximation). The fracture is long and thin meaning $\epsilon = h_0/L \ll 1$ and $\alpha = dh/dx = [h(L) - h_0]/L = \Delta h/L \ll 1$, where $h_0 = h(0)$. Gravity is neglected but, in these schematics, it would act in the transversely in the negative $y$-direction. The flow is symmetric about the centerline $z = 0$, and primarily in the $x$-direction, along the fracture. The top and bottom walls $z = \pm h(x)$ are permeable (permeability $k_w$) and allow a non-zero vertical velocity component $v_w$ at the wall, which is to be determined.

**Table 1**
Typical dimensions of a hydraulic fracture and typical values of the dimensionless parameters of the hydraulic conductivity model derived in this study.

| Quantity | Notation | Value | Remarks |
|---|---|---|---|
| Fracture total length | $L_{\text{total}}$ | $100 \sim 1000$ m | Barbati et al. [4] |
| Fracture width | $w$ | $10 \sim 100$ m | Barbati et al. [4] |
| Fracture gap/aperture | $h_0$ | $2 \sim 10$ mm | Barbati et al. [4] |
| Typical velocity | $U_0$ | $\lesssim 10^{-3}$ m s$^{-1}$ | Yew and Weng [64, Ch. 1] |
| Permeability of the wall | $k_w$ | $\lesssim 5 \times 10^{-13}$ m$^2$ | Barbati et al. [4] |
| Hele-Shaw shape variation | $\delta = \alpha/\epsilon$ | $\lesssim 10^{-1}$ | Slow variation assumption |
| Hele-Shaw aspect ratio | $\epsilon = h_0/L$ | $10^{-4} \sim 10^{-2}$ | Using $L = L_{\text{total}}/100$ |
| Hele-Shaw slope | $\alpha = dh/dx$ | $\lesssim 10^{-3}$ | Using $\lvert\alpha\rvert \sim \epsilon\delta$ |
| Wall slip coeff. | $\phi = \sqrt{k_w}/(ah_0)$ | $\lesssim 10^{-3}$ | $a = 0.1$ |
| Reduced Reynolds number | $\tilde{R}e = \rho U_0 h_0^2/(\mu L)$ | $\lesssim 0.1$ | $\rho$, $\mu$ for water |

constant-height channel using the idealized boundary condition of equal prescribed wall-normal velocities. Since then, a large literature has addressed many variations on this problem, including asymmetric wall normal velocities [55], flow development effects [12], unsteadiness [28], and so on. These works rely on reducing the problem to a nonlinear ordinary differential equation, owing to the existence of a similarity transformation in two dimensions (2D). Unfortunately, this technique does *not* work in the case of a aperture gradient, such as the present geometry with $h = h(x)$; instead a perturbation solution must be sought [20, 61]. Kumar et al. [29] showed that a similar situation arises if the geometry is uniform but the slip length varies in the flow-wise direction, i.e., $\ell_{\text{slip}} = \ell_{\text{slip}}(x)$. Importantly, imposing the wall-normal velocity *a priori* is a significant limitation of the previous studies because, as Conlisk notes, "[t]he suction velocity at the wall ... must be calculated from the properties of the porous medium" [14, p. 162]. Here, we take the perturbative mathematical approach, based on the notion of *slow variation* in fluid mechanics [59], to calculate the conductivity of a shaped fracture with permeable walls.

Beavers and Joseph [6] experimentally characterized pressure-driven (Poiseuille) flow over a naturally permeable surface (i.e., channel flow with porous walls) and proposed a boundary condition to account for the wall permeation. Specifically, they showed that the shear stress balance at the fluid–solid interface can be represented by a first-order (partial) slip boundary condition with slip length $\ell_{\text{slip}} = \sqrt{k_w}/a$, where $k_w$ is the permeability of the porous wall, and $a$ is a dimensionless constant determined by the structure of the material, ranging from 0.1 to 4.0 [6]. Taylor [54] observed that $a$ is not a universal value, but rather it depends on the flow geometry. Saffman [49] substantiated this observation and generalized the slip condition to arbitrary surfaces. However, this correction only affects the already empirically-determined slip length, thus the form of the boundary condition remains unchanged, while $a \approx 0.1$ is in good agreement with most experiments [7]. Zhang and Prosperetti [65] provided further evidence for the slip boundary condition via pore-scale direct numerical simulations of a two-dimensional channel flow. A more detailed discussion of the history and mathematical foundations of the partial slip boundary condition

can be found in [39, 11]. Now, define the dimensionless quantity $\phi = \ell_{\text{slip}}/h_0$ as the slip coefficient. For the typical dimensions of a hydraulically-driven fracture, we estimate the dimensionless parameters values in Table 1.

To address the issue that fracture walls in the subsurface are themselves porous media, Mohais et al. [33, 34] employed the Beavers–Joseph boundary condition to solve for the flow in, and obtain a correction for the conductivity $\mathcal{K}$ of, uniform-aperture fractures with permeable walls. So far, however, a theory for the conductivity of variable-aperture fractures with porous walls (the most common case in the subsurface) is lacking. This study aims to fill this knowledge gap. Importantly, we also validate our proposed model for $\mathcal{K}$ against direct numerical simulations using a custom solver built on OpenFOAM® [62, 56]. We provide an implementation of the *semi-implicit method for pressure-linked equations* (SIMPLE) algorithm (see, e.g., [36, Ch. 15]) for the Navier–Stokes equations subject to the tensorial form of the Beavers–Joseph–Saffman (BJS) boundary condition.

## 2. Mathematical analysis

### 2.1. Governing equations

The flow geometry and notation are shown in Fig. 1. An incompressible Newtonian fluid of density $\rho$ and dynamic viscosity $\mu$ fills the gap. The fracture is long and thin, which justifies taking $h(x)$ to be a linear function [38]. Alternatively, one is allowed to substitute $\alpha = \alpha(x)$ in the results below if $dh/dx \neq const.$, as long as $\max_x \alpha(x)$ satisfies the original smallness assumption [66, 61]. Let $U_0$ be the average inlet velocity at the inlet ($x = 0$), which serves as the scale for the horizontal velocity $u(x, z)$ in the fracture. The flow is assumed to be 2D, i.e., the fracture is infinite in the transverse $y$-direction. Then, conservation of mass requires that the scale for the vertical velocity $v(x, z)$ be $V_0 = U_0 h_0/L = \epsilon U_0$ [14, Sec. 4.9].

Now, we define the dimensionless (starred) variables

$$\begin{gathered} x^* = x/L, \quad z^* = z/h_0, \quad h^*(x^*) = h(x)/h_0, \\ u^*(x^*, z^*) = u(x, z)/U_0, \quad v^*(x^*, z^*) = v(x, z)/V_0, \\ p^*(x^*, z^*) = \epsilon h_0 p(x, z)/(\mu U_0), \quad \mathcal{K}^*(x^*) = \mathcal{K}(x)/h_0^2, \end{gathered} \tag{1}$$

where $Re = \rho U_0 h_0/\mu$ is the Reynolds number and $\tilde{Re} = \epsilon Re$ is a reduced Reynolds number [66]. Then, the dimensionless conservation of mass and momentum equations are

$$\frac{\partial u^*}{\partial x^*} + \frac{\partial v^*}{\partial z^*} = 0, \tag{2a}$$

$$\tilde{Re}\left(u^*\frac{\partial u^*}{\partial x^*} + v^*\frac{\partial u^*}{\partial z^*}\right) = -\frac{\partial p^*}{\partial x^*} + \epsilon^2\frac{\partial^2 u^*}{\partial x^{*2}} + \frac{\partial^2 u^*}{\partial z^{*2}}, \tag{2b}$$

$$\epsilon^2\tilde{Re}\left(u^*\frac{\partial v^*}{\partial x^*} + v^*\frac{\partial v^*}{\partial z^*}\right) = -\frac{\partial p^*}{\partial z^*} + \epsilon^4\frac{\partial^2 v^*}{\partial x^{*2}} + \epsilon^2\frac{\partial^2 v^*}{\partial z^{*2}}, \tag{2c}$$

subject to the following boundary conditions (BCs):

$$\text{symmetry at } z^* = 0: \qquad \frac{\partial u^*}{\partial z^*} = 0 \text{ and } v^* = 0; \tag{3a}$$

$$\text{partial slip at } z^* = h^*: \qquad u^* = -\phi\frac{\partial u^*}{\partial z^*}, \tag{3b}$$

where $\phi$ is the slip coefficient, and $h^* = h^*(x^*) = 1 + \alpha x^*/\epsilon$. Observe that, here, we can introduce $\delta = \alpha/\epsilon = [h(L) - h(0)]/h_0 = \Delta h/h_0$, which is the percent change of $h(x)$ over the typical fracture variation length $L$, so that $h^*(x^*) = 1 + \delta x^*$. The assumption of *slow variation* dictates that $\delta \ll 1$, while the assumption of *lubrication* (small aspect ration) dictates that $\epsilon = h_0/L \ll 1$ (see also [14, 66]). These two assumptions are independent and lead to $\alpha = \epsilon\delta \lll 1$, which is typical of fractures, as discussed in Sec. 1.

The BC in Eq. (3a) is the centerline symmetry condition, while the BC in Eq. (3b) comes from the BJS partial slip BC [6, 7, 49, 31, 25] on the permeable wall (see Supplementary Material for details). Physically, the BJS BC enforces a shear stress balance along the fluid–porous solid interface by relating the tangential velocity component to the normal component of the velocity gradient via the slip coefficient $\phi$ (which is an empirically-measurable constant set by the permeability of the surrounding medium and its pore geometry, recall Sec. 1). Importantly, the BJS BC allows us to solve for the flow in the fracture without solving for the flow in the surround porous medium.

### 2.2. Perturbation solution for the velocity profile

Following the standard procedure of a regular perturbation expansion [22], the velocity field is expanded as $u^* = u_0^* + \tilde{Re}\, u_1^* + \cdots$ and $v^* = v_0^* + \tilde{Re}\, v_1^* + \cdots$ ($\tilde{Re} \ll 1$). Then, we find the horizontal velocity at the leading order (see Supplementary Material for details):

$$u_0^*(x^*, z^*) = \left(\frac{h^{*2} - z^{*2}}{2} + \phi h^*\right)\left(-\frac{dp^*}{dx^*}\right). \tag{4}$$

Since the flow is in the direction of positive $x^*$, $dp^*/dx^* < 0$. Then, the leading-order depth-averaged velocity is

$$\begin{aligned} \langle u_0^*\rangle(x^*) &= \frac{1}{h^*(x^*)}\int_0^{h^*(x^*)} u_0^*(x^*, z^*)\, dz^* \\ &= \frac{3\phi h^* + h^{*2}}{3}\left(-\frac{dp^*}{dx^*}\right). \end{aligned} \tag{5}$$

And, the vertical velocity at the leading order is

$$\begin{aligned} v_0^*(x^*, z^*) = \left(h^* + \phi\right)\frac{dh^*}{dx^*}z^*\frac{dp^*}{dx^*} \\ - \left(\frac{z^{*2}}{6} - \frac{h^{*2}}{2} - \phi h^*\right)z^*\frac{d^2p^*}{dx^{*2}}. \end{aligned} \tag{6}$$

At the next order in $\tilde{Re}$, we find the depth-averaged velocity's correction:

$$\langle u_1^*\rangle(x^*) = \left(\frac{3}{35}h^{*2} + \frac{\phi}{3}h^* + \frac{\phi^2}{3}\right)h^{*4}\left(-\frac{dp^*}{dx^*}\right)\frac{d^2p^*}{dx^{*2}}$$

$$-\left(\frac{h^*}{5}+\frac{\phi}{3}\right)h^{*3}(h^*+\phi)\frac{1}{\epsilon}\frac{dh^*}{dx^*}\left(\frac{dp^*}{dx^*}\right)^2. \quad (7)$$

For the present purposes, it is not necessary to write out $u_1^*$ and $v_1^*$ but they can be calculated (see Supplementary Material).

### 2.3. Equivalent Darcy's law and the hydraulic conductivity

To obtain the conductivity $\mathcal{K}$ in a shaped fracture with porous walls, we must put the flow field thus obtained into the form of a Darcy-like law, i.e., $\langle u^*\rangle \propto -dp^*/dx^*$, with the proportionality factor being the sought-after result. To this end, combining Eqs. (5) and (7) we obtain the "full" depth-average horizontal velocity up to $\mathcal{O}(\tilde{Re})$: $\langle u^*\rangle = \langle u_0^*\rangle + \tilde{Re}\langle u_1^*\rangle$. However, at this point, the pressure distribution $p^*(x^*)$ is still *unknown*. To close the problem, we need another constraint. Mohais et al. [34] provided one solution by assuming a *constant* permeation velocity $v_w$ in a parallel fracture ($\alpha = dh^*/dx^* = 0$, $h^* = 1$), i.e., $v_0\big|_{z=\pm h_0} = \pm v_w$. We could apply this BC here too (see Supplementary Material), however, as discussed in Sec. 1, the assumption of a constant $v_w$ is not suitable for shaped fractures, due to the flow-wise $x^*$-variation of the aperture.

Instead, to close the problem, we impose the full flux onto the leading-order depth-averaged velocity, i.e., we set $\langle u_0^*\rangle = 1$. We impose this condition because, as discussed in Sec. 1, the representative fracture region of interest is away from the crack tip, and thus the flow is not leak-off dominated, following Refs. [33, 34, 53, 61] but in contrast to Refs. [64, 4, 50] (or, e.g., Refs. [58, 21] in the context of filtration). Thus, $v_w^*$ will *not* be constant and will be self-consistently determined as a function of $x^*$. Another modeling approach is to set the wall-normal velocity via the local pressure, as in filtration problems [58, 21], however this approach is beyond the scope of the present study focused on porous media flows.

Applying the constraint $\langle u_0^*\rangle = 1$ to Eq. (5), we compute $dp^*/dx^*$ and $d^2p^*/dx^{*2}$ (see Supplementary Material). Substituting the latter results into Eq. (7) and putting it all together,

$$\begin{aligned}\langle u^*\rangle &= -\mathcal{K}^*\frac{dp^*}{dx^*},\\ \mathcal{K}^*(x^*) &= \left[\frac{3\phi h^*+h^{*2}}{3}-\tilde{Re}\frac{h^{*3}(28\phi^2+22\phi h^*+3h^{*2})\delta}{35(3\phi+h^*)^2}\right],\end{aligned} \quad (8)$$

which is already in the form of Darcy's law. Finally, Eq. (8) can be put in dimensional form:

$$\langle u\rangle = -\frac{\mathcal{K}}{\mu}\frac{\partial p}{\partial x}, \qquad \mathcal{K} = \frac{h_0^2}{3}C, \quad (9)$$

where we have defined the dimensionless function

$$\begin{aligned}C(x) &= \left[3\phi h^*+h^{*2}-3\tilde{Re}\frac{h^{*3}(28\phi^2+22\phi h^*+3h^{*2})\delta}{35(3\phi+h^*)^2}\right]\\ &= \underbrace{1}_{\text{(I)}}+\underbrace{3\phi}_{\text{(II)}}+\underbrace{\left[(2+3\phi)\frac{x}{L}-3\tilde{Re}\,\frac{3+22\phi+28\phi^2}{35(3\phi+1)^2}\right]\delta}_{\text{(III)}}\\ &\quad+\mathcal{O}\left(\delta^2\right)\end{aligned} \quad (10)$$

to represent the "correction" to the hydraulic conductivity of the fracture. As discussed in Sec. 1, typical fractures are long and shallow ($\epsilon \ll 1$), and the slopes of the wall variation are even smaller ($\alpha = \epsilon\delta \lll 1$), thus we expanded a number of terms in Eq. (10) into Taylor series and kept only terms up to $\mathcal{O}(\delta)$ to highlight the key physical effects of shape variation in a fracture with permeable walls.

The function $C$ accounts for wall permeation through the BJS slip coefficient $\phi = \sqrt{k_w}/(ah_0)$, the shape of the fracture through the slope $\alpha = dh/dx$ and aspect ratio $\epsilon = h_0/L$, and weak inertia through the reduced Reynolds number $\tilde{Re} = \rho U_0 h_0^2/(\mu L)$. The first term (I) on the right-hand side of Eq. (10) corresponds to the classic conductivity calculated by the Hele-Shaw analogy [5]; the second term (II) comes from wall permeation [34]; the third term (III), which is the novel contribution of our calculation, and is explicitly a function of the flow-wise coordinate $x$, is due to the *coupled* effect of geometry variation, fluid inertia, and wall permeation.

### 2.4. Wall permeation velocity

Substituting the expression for $dp^*/dx^*$ into the vertical velocity from Eq. (6), and evaluating the result at $z^* = h^*$, we obtain the *a priori* unknown wall permeation velocity

$$v_w(x) = -V_0\frac{h(x)\delta}{3\phi h_0+h(x)}. \quad (11)$$

Recall that $\alpha < 0$ ($\Rightarrow \delta < 0$), so $v_w > 0$, i.e., the velocity is *into* the wall. Observe that both $v_w$ and the term (III) in $C$ vanish for $\alpha = 0$ ($\Rightarrow \delta = 0$) (parallel walls) because, in this case, there is no driving force to push fluid into the porous walls. We have imposed the full volumetric flux onto the leading-order solution (see also [53]), and it must be conserved. Note $v_w \neq 0$ for $\phi = 0$ because there can still be fluid penetrating the wall in the normal direction even if there is no (tangential) slip. The permeation velocity for $\phi = 0$ is driven by the flow-wise contraction of the aperture (rather than being imposed *a priori* [34]).

## 3. Results and Discussion

Figure 2 shows the flow profile generated from the perturbative solution from Sec. 2, for a fracture with linear aperture variation. The streamlines highlight the 2D nature of the velocity field, as well as permeation through the fracture's top wall. The pressure does not vary with $z^*$, as required by the lubrication (small aspect ratio, $\epsilon \ll 1$) approximation.

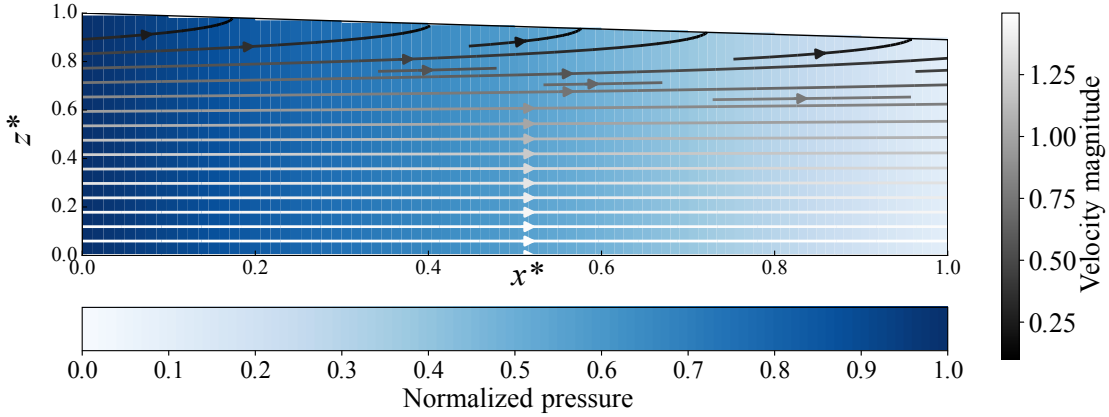


**Figure 2:** Illustration of the dimensionless analytical flow solution (Eqs. (4), (5) and (6)) obtained for the model shaped fracture with permeable angled walls. Only the top half ($0 \le z^* \le 1$) is shown, for clarity. Background color denotes pressure, and curves are streamlines shaded by velocity magnitude. Here, $\alpha = -10^{-3}$, $\epsilon = 0.01$, $\tilde{Re} = 0.01$, $\phi = 10^{-3}$.

Next, we validate our mathematical results against "full" Navier–Stokes direct numerical simulations (DNS) [3]. We carried out DNS using the simpleFoam solver in OpenFOAM® ver. 7.0 [62, 56], an open-source library based on the *finite volume method* [36]. The simulations (see Supplementary Material for description of the method) were performed using the Hele-Shaw cell geometry with varying aperture along $x$ from Fig. 1. Importantly, unlike previous computational studies on flow in fractures with permeable walls [57], we did *not* impose the wall (tangent and normal) velocities from the theory onto the simulations. The latter approach is akin to verification, while we seek validation [47] between theory and simulation. Instead, we imposed a tensorial slip condition on the tangential velocity (the BJS BC) coupled with a normal pressure flux BC, to allow the simulation to self-consistently determine the flow (in particular, the unknown wall permeation velocity) and pressure profiles.

The DNSs provide the 2D velocity field and the pressure distribution, i.e., $\big(u^*(x^*, z^*), v^*(x^*, z^*)\big)$ and $p^*(x^*, z^*)$ (both scaled as in Eq. (1)). From these quantities, the volumetric flux across a vertical cross-section and the pressure gradient at a given $x^*$ are computed, yielding $\langle u^*(x^*)\rangle$ and $dp^*/dx^*$. Their ratio, $\langle u^*\rangle/(-dp^*/dx^*)$ is to be compared to the theoretically predicted dimensionless hydraulic conductivity $\mathcal{K}^*(x^*)$ from Eq. (8).

First, in Fig. 3, we show the velocity profiles across the midlength plane ($x^* = 0.5$) of fractures with different slopes. The simulation results agree well with theory. The zoomed-in inset in Fig. 3(a) highlights that $u^*$ does not start from 0, but rather some finite value, as required by the BJC partial slip BC. For all $\alpha$, $v^* = 0$ at the centerline ($z^* = 0$) as required by symmetry, then increases smoothly in absolute value towards the walls (Fig. 3(b)). Fluid enters into the surrounding porous medium and the wall permeation velocity $v_w^* = v^*|_{z^*=h^*}$ is self-consistently computed (shown in Supplementary Material Fig. S.7). The wall permeation velocity increases with $|\alpha|$ to maintain the imposed flux through these narrowing fractures. Meanwhile, for $\alpha = 0$, $v^* = 0$ for all $z^*$, i.e., there is no permeation into the porous medium, only slip at the fluid–solid interfaces ($z^* = \pm 1$).

To verify the derived analytical expression for the hydraulic conductivity in a shaped fracture, we compute $\mathcal{K}^*(x^*)$ in multiple angled fractures with permeable walls, based on typical reservoir properties summarized in Table 1. Figure 4(a) shows the predicted $\mathcal{K}^*$ (from theory) against the simulated $\mathcal{K}^*$ values along the fracture (multiple $x^*$ for each) for multiple slope values $\alpha$, and multiple slip coefficients $\phi$, for fixed $\tilde{Re}$. In the same color family, the brightness of the color refers to the value of $\phi$: the darker the color, the smaller $\phi$ is. The classical conductivity $\mathcal{K} = 1/3$ (i.e., for $\alpha = \phi = 0$) calculated from the Hele-Shaw analogy [5, 66] is shown by • (simulated) and — (predicted). All data points in Fig. 4(a) lie close to the line of slope 1, which means that the predicted conductivity (from theory) is in good agreement with the simulations. For $\phi > 10^{-3}$, the correlated trend continues, but in these cases the slip length is large and the single-domain simulation approach is not appropriate (the flow in the surrounding porous medium should be resolved as well to be able to impose suitable BCs numerically).

In Fig. 4(b), we plot the conductivity variation along the flow-wise ($x^*$) direction, a novel prediction of the present theory. By comparing the conductivity for the same $\alpha$ but different $\phi$, for example, $\alpha = -10^{-3}$ (the red color family), we observe that wall slip has only a weak effect on $\mathcal{K}^*$. By comparing the conductivity for different $\alpha$ (different color families), we observe that $\mathcal{K}^*$ decreases with $x^*$, which means that it becomes "harder" for the fluid to flow through the narrowing fractures. Of course this is expected on physical grounds, but this effect of $\alpha$ on $\mathcal{K}^*$ had not been quantified prior to this study. In particular, our results in Fig. 4 show that that even weak slopes have a much more significant impact on the conductivity, than wall slip due to the permeability of the walls. Likewise, the wall permeation velocity $v_w^*$ has *not* been *a priori* specified, and is also a strong function of $\alpha$ (recall Sec. 2.4 and Supplementary Material Fig. S.7).

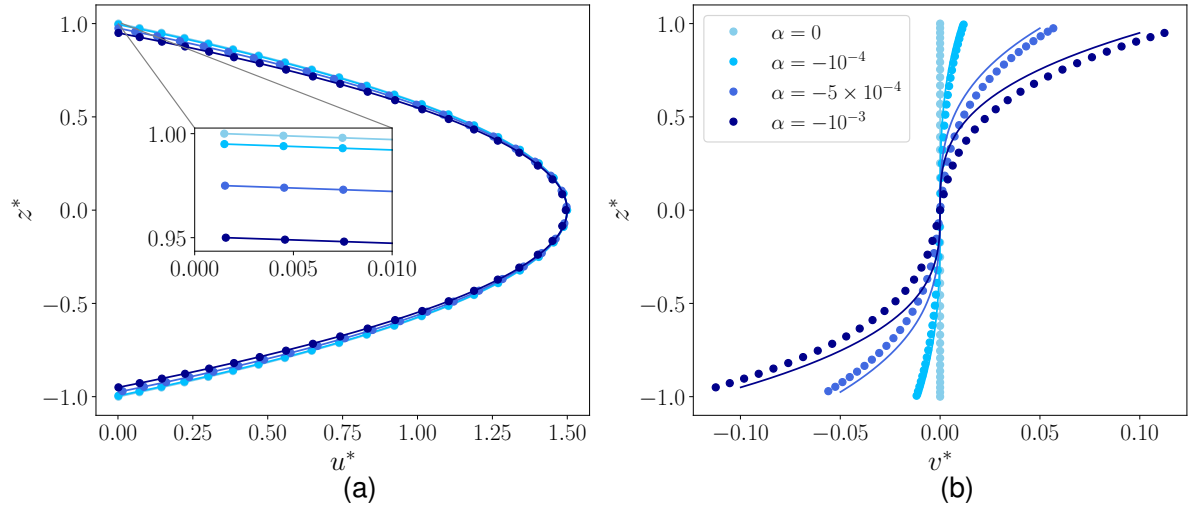


**Figure 3:** Dimensionless velocity profiles across the fracture aperture $z^*$, at the mid-fracture plane $x^* = 0.5$, for $\phi = 5 \times 10^{-4}$ and $\tilde{Re} = 0.01$: (a) the horizontal component $u^*(x^*, z^*)$ (inset highlights the non-zero slip velocity at the wall); (b) the vertical component $v^*(x^*, z^*)$. Solid curves are the theoretical profiles from Eq. (6), and filled circles with the same colors are the corresponding simulation results. Colors represent different $\alpha$ values (see legend).

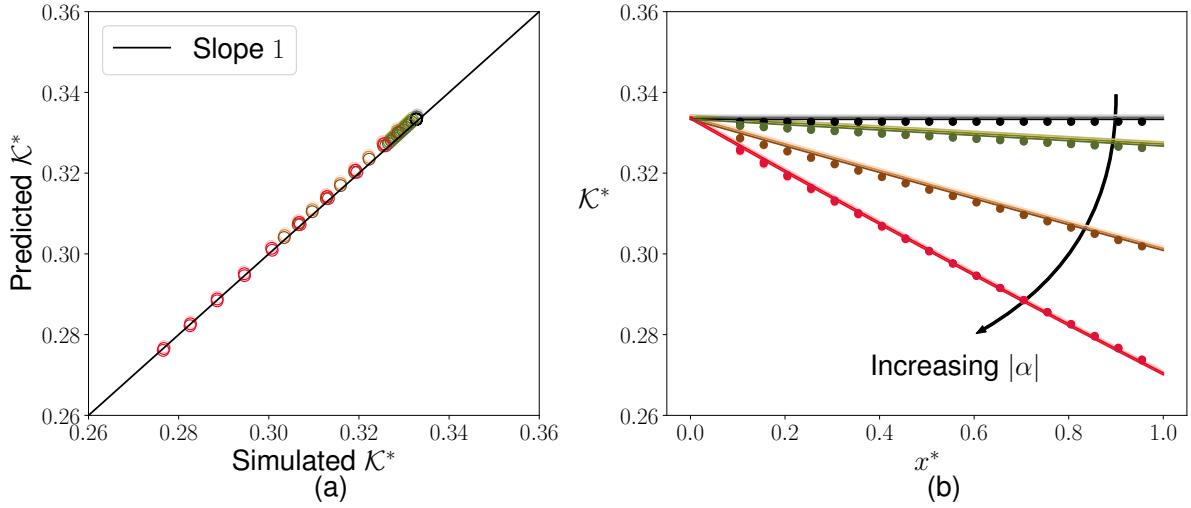


**Figure 4:** The dimensionless conductivity $\mathcal{K}^*$ of shaped fractures, for different slip coefficients $\phi$ and wall slopes $\alpha$: (a) correlation plot of predicted $\mathcal{K}^*$ values from Eq. (8) versus simulated $\mathcal{K}^*$ values; (b) the variation of $\mathcal{K}^*(x^*)$ along the fracture length. Colors represent cases with different $\alpha$ and $\phi$ values: ●●●: $\alpha = 0$, $\phi \in \{0, 5 \times 10^{-4}, 10^{-3}\}$; ●●●: $\alpha = -10^{-4}$, $\phi \in \{0, 5 \times 10^{-4}, 10^{-3}\}$; ●●●: $\alpha = -5 \times 10^{-3}$, $\phi \in \{0, 5 \times 10^{-4}, 10^{-3}\}$; ●●●: $\alpha = -10^{-3}$, $\phi \in \{0, 5 \times 10^{-4}, 10^{-3}\}$. In (b), filled circles represent the simulation results, and solid curves of the same color represent the corresponding theoretical prediction Eq. (10) with $\tilde{Re} = 0.01$.

## 4. Conclusions and Outlook

The contribution of this study is the mathematical expressions, Eqs. (9) and (10), that relate the fracture conductivity to the geometric and physical quantities, and which explicitly shows the coupling between the fracture shape (in terms of its wall angle), the permeability of the porous wall (in terms of the Beavers–Joseph–Saffman slip length), and the inertia of the fluid in the fracture (in terms of a Reynolds number). Additionally, unlike previous studies on fractures with permeable walls, we self-consistently determined the wall permeation velocity, Eq. (6), which is *a priori* unknown and is set by the balance of pressure forces pushing fluid into the walls, and the permeability of the surrounding matrix. From these results, we concluded that the coupling effect of geometric variation, wall permeation and inertia leads to a decreasing conductivity along a narrowing fracture. Importantly, what has not been appreciated in previous studies is that, among these factors, the geometric variation (specifically, the resistance to flow induced by the narrowing of a fracture) dominates the conductivity change, even for slow shape variation (small slopes). The theory was validated against direct numerical simulation of the Navier–Stokes equations in a model Hele-Shaw geometry.

In future work, the analytical solutions derived could be used to improve systems-level (network) modelling of hy-

draulic fracturing and transport [19], wherein simple modifications of Darcy's law are currently used to capture the geometric variation and wall permeability [10]. As mentioned above, our analysis is easily applied to fractures with other (more complex but still "slow") types of geometric variations, such those considered in [61]. It could also be worthwhile to analyze a pressure-controlled flow scenario. The theory is straightforward to extend: imposing a Darcy-like BC, such as $v_w^* \propto p^* - p_{\mathrm{ref}}^*$ (for some reference pressure $p_{\mathrm{ref}}^*$ deep in the surrounding porous medium) [58, 21, 50], Eq. (6) yields a dimensionless ODE for the pressure, on which one can impose an inlet and outlet pressure. In this context, the OpenFOAM® solver developed could also be adapted to account for solute non-Fickian transport into the surround rock, as well as wall reactions [37]. Our results could also guide the design of microfluidic analogues of porous media flows [52] for emerging reservoir-on-a-chip technologies [30] meant to emulate flow in geophysical reservoirs [44]. Additionally, our solutions for the wall permeation velocity can be employed to estimate leakage in near-well operations, which can improve the accuracy of reservoir simulations [16]. Our analytical flow solution could also be used to revisit the effect of wall permeation on the Saffman–Taylor (viscous fingering) instability in angled Hele-Shaw cells [1, 2].

## Research data availability

The OpenFOAM® solver, example simulation configuration files, and post-processing scripts are freely available at https://doi.org/10.5281/zenodo.3934416. [University of Illinois/NCSA Open Source License].

## CRediT authorship contribution statement

**Daihui Lu:** Conceptualization, Data curation, Formal analysis, Investigation, Methodology, Validation, Visualization, Writing. **Federico Municchi:** Investigation, Methodology, Software, Supervision, Validation, Writing. **Ivan C. Christov:** Conceptualization, Funding acquisition, Formal analysis, Project administration, Supervision, Writing.

## References


[1] Al-Housseiny, T.T., Stone, H.A., 2013. Controlling viscous fingering in tapered Hele-Shaw cells. Phys. Fluids 25, 092102. doi:10.1063/1.4819317.

[2] Al-Housseiny, T.T., Tsai, P.A., Stone, H.A., 2012. Control of interfacial instabilities using flow geometry. Nat. Phys. 8, 747–750. doi:10.1038/nphys2396.

[3] Al-Yaarubi, A.H., Pain, C.C., Grattoni, C.A., Zimmerman, R.W., 2013. Navier-Stokes simulations of fluid flow through a rock fracture, in: Faybishenko, B., Witherspoon, P.A., Gale, J. (Eds.), Dynamics of Fluids and Transport in Fractured Rock. American Geophysical Union, Washington, DC. volume 162 of *Geophysical Monograph Series*, pp. 55–64. doi:10.1029/162GM07.

[4] Barbati, A.C., Desroches, J., Robisson, A., McKinley, G.H., 2016. Complex fluids and hydraulic fracturing. Annu. Rev. Chem. Biomol. Eng. 7, 415–453. doi:10.1146/annurev-chembioeng-080615-033630.

[5] Bear, J., 1972. Dynamics of Fluids in Porous Media. Environmental Science, American Elsevier Publishing Company, Inc., New York, NY.

[6] Beavers, G.S., Joseph, D.D., 1967. Boundary conditions at a naturally permeable wall. J. Fluid Mech. 30, 197–207. doi:10.1017/S0022112067001375.

[7] Beavers, G.S., Sparrow, E.M., Magnuson, R.A., 1970. Experiments on coupled parallel flows in a channel and a bounding porous medium. ASME J. Basic Eng. 92, 843–848. doi:10.1115/1.3425155.

[8] Berkowitz, B., 1989. Boundary conditions along permeable fracture walls: Influence on flow and conductivity. Water Res. Res. 25, 1919–1922. doi:10.1029/WR025i008p01919.

[9] Berman, A.S., 1953. Laminar flow in channels with porous walls. J. Appl. Phys. 24, 1232–1235. doi:10.1063/1.1721476.

[10] Birdsell, D.T., Rajaram, H., Dempsey, D., Viswanathan, H.S., 2015. Hydraulic fracturing fluid migration in the subsurface: A review and expanded modeling results. Water Res. Res. 51, 7159–7188. doi:10.1002/2015WR017810.

[11] Bottaro, A., 2019. Flow over natural or engineered surfaces: an adjoint homogenization perspective. J. Fluid Mech. 877, P1. doi:10.1017/jfm.2019.607.

[12] Brady, J.F., 1984. Flow development in a porous channel and tube. Phys. Fluids 27, 1061. doi:10.1063/1.864735.

[13] Brown, S.R., 1987. Fluid flow through rock joints: The effect of surface roughness. J. Geophys. Res. 92, 1337–1347. doi:10.1029/JB092iB02p01337.

[14] Conlisk, A.T., 2012. Essentials of Micro- and Nanofluidics with Applications to the Biological and Chemical Sciences. Cambridge University Press, New York, NY.

[15] Detournay, E., 2016. Mechanics of hydraulic fractures. Annu. Rev. Fluid Mech. 48, 311–339. doi:10.1146/annurev-fluid-010814-014736.

[16] Dumkwu, F.A., Islam, A.W., Carlson, E.S., 2012. Review of well models and assessment of their impacts on numerical reservoir simulation performance. J. Petrol. Sci. Eng. 82-83, 174–186. doi:10.1016/j.petrol.2011.12.005.

[17] Garagash, D., Detournay, E., 1999. The tip region of a fluid-driven fracture in an elastic medium. ASME J. Appl. Mech. 67, 183–192. doi:10.1115/1.321162.

[18] van Golf-Racht, T.D., 1982. Fundamentals of Fractured Reservoir Engineering. volume 12 of *Developments in Petroleum Science*. 1st ed., Elsevier Scientific Publishing Company, Amsterdam, The Netherlands. doi:10.1016/S0376-7361(08)70330-3.

[19] Gostick, J., Aghighi, M., Hinebaugh, J., Tranter, T., Hoeh, M.A., Day, H., Spellacy, B., Sharqawy, M.H., Bazylak, A., Burns, A., Lehnert, W., Putz, A., 2016. OpenPNM: A pore network modeling package. Comput. Sci. Eng. 18, 60–74. doi:10.1109/MCSE.2016.49.

[20] Grotberg, J.B., 1984. Volume-cycled oscillatory flow in a tapered channel. J. Fluid Mech. 141, 249–264. doi:10.1017/S0022112084000823.

[21] Herterich, J.G., Vella, D., Field, R.W., Hankins, N.P., Griffiths, I.M., 2015. Tailoring wall permeabilities for enhanced filtration. Phys. Fluids 27, 053102. doi:10.1063/1.4919658.

[22] Holmes, M.H., 2013. Introduction to Perturbation Methods. volume 20 of *Texts in Applied Mathematics*. 2 ed., Springer Science+Business Media, New York, NY. doi:10.1007/978-1-4614-5477-9.

[23] Hyman, J.D., Jiménez-Martínez, J., Viswanathan, H.S., Carey, J.W., Porter, M.L., Rougier, E., Karra, S., Kang, Q., Frash, L., Chen, L., Lei, Z., O'Malley, D., Makedonska, N., 2016. Understanding hydraulic fracturing: a multi-scale problem. Phil. Trans. R. Soc. A 374, 20150426. doi:10.1098/rsta.2015.0426.

[24] Iliev, O., Mikelić, A., Popov, P., 2008. On upscaling certain flows in deformable porous media. Multiscale Model. Simul. 7, 93–123. doi:10.1137/06067732X.

[25] Jäger, W., Mikelić, A., 2000. On the interface boundary condition of Beavers, Joseph, and Saffman. SIAM J. Appl. Math. 60, 1111–1127. doi:10.1137/S003613999833678X.

[26] Jin, Y., Dong, J., Zhang, X., Li, X., Wu, Y., 2017. Scale and size ef-

fects on fluid flow through self-affine rough fractures. Int. J. Heat Mass Transfer 105, 443–451. doi:10.1016/j.ijheatmasstransfer.2016.10.010.

[27] Karra, S., Makedonska, N., Viswanathan, H.S., Painter, S.L., Hyman, J.D., 2015. Effect of advective flow in fractures and matrix diffusion on natural gas production. Water Res. Res. 51, 8646–8657. doi:10.1002/2014WR016829.

[28] King, J.R., Cox, S.M., 2001. Asymptotic analysis of the steady-state and time-dependent Berman problem. J. Eng. Math. 39, 87–130. doi:10.1023/A:1004824527547.

[29] Kumar, A., Datta, S., Kalyanasundaram, D., 2016. Permeability and effective slip in confined flows transverse to wall slippage patterns. Phys. Fluids 28, 082002. doi:10.1063/1.4959184.

[30] Kumar Gunda, N.S., Bera, B., Karadimitriou, N.K., Mitra, S.K., Hassanizadeh, S.M., 2011. Reservoir-on-a-Chip (ROC): A new paradigm in reservoir engineering. Lab Chip 11, 3785. doi:10.1039/c1lc20556k.

[31] Layton, W.J., Schieweck, F., Yotov, I., 2002. Coupling fluid flow with porous media flow. SIAM J. Numer. Anal. 40, 2195–2218. doi:10.1137/S0036142901392766.

[32] McBride, J., Aly Sergie, M., 2015. Hydraulic Fracturing (Fracking). Technical Report. Council on Foreign Relations. URL: https://www.cfr.org/backgrounder/hydraulic-fracturing-fracking.

[33] Mohais, R., Xu, C., Dowd, P., 2011. Fluid flow and heat transfer within a single horizontal fracture in an enhanced geothermal system. ASME J. Heat Transfer 133, 112603. doi:10.1115/1.4004369.

[34] Mohais, R., Xu, C., Dowd, P.A., Hand, M., 2012. Permeability correction factor for fractures with permeable walls. Geophys. Res. Lett. 39, L03403. doi:10.1029/2011GL050519.

[35] Mohais, R., Xu, C., Dowd, P.A., Hand, M., 2016. Enhanced Geothermal Systems, in: Lehr, J.H., Keeley, J., Kingery, T.B. (Eds.), Alternative Energy and Shale Gas Encyclopedia. Wiley, Hoboken, NJ. Wiley Series on Energy. chapter 27, pp. 265–289. doi:10.1002/9781119066354.ch27.

[36] Moukalled, F., Mangani, L., Darwish, M., 2016. The Finite Volume Method in Computational Fluid Dynamics: An Advanced Introduction with OpenFOAM® and Matlab. Fluid Mechanics and its Applications, Springer International Publishing, Cham, Switzerland. doi:10.1007/978-3-319-16874-6.

[37] Municchi, F., Icardi, M., 2020. Macroscopic models for filtration and heterogeneous reactions in porous media. Adv. Water. Res. 141, 103605. doi:10.1016/j.advwatres.2020.103605.

[38] Nicholl, M.J., Rajaram, H., Glass, R.J., Detwiler, R., 1999. Saturated flow in a single fracture: evaluation of the Reynolds Equation in measured aperture fields. Water Res. Res. 35, 3361–3373. doi:10.1029/1999WR900241.

[39] Nield, D.A., Bejan, A., 2013. Mechanics of Fluid Flow Through a Porous Medium, in: Convection in Porous Media. 4 ed.. Springer Science+Business Media, New York, NY. chapter 1, pp. 1–29. doi:10.1007/978-1-4614-5541-7{_}1.

[40] Olasolo, P., Juárez, M.C., Morales, M.P., D'Amico, S., Liarte, I.A., 2016. Enhanced geothermal systems (EGS): A review. Renew. Sust. Energ. Rev. 56, 133–144. doi:10.1016/j.rser.2015.11.031.

[41] Osiptsov, A.A., 2017. Fluid mechanics of hydraulic fracturing: A review. J. Petrol. Sci. Eng. 156, 513–535. doi:10.1016/j.petrol.2017.05.019.

[42] Patzek, T.W., Male, F., Marder, M., 2013. Gas production in the Barnett Shale obeys a simple scaling theory. Proc. Natl Acad. Sci. USA 110, 19731–19736. doi:10.1073/pnas.1313380110.

[43] Phillips, O.M., 1991. Flow and Reactions in Permeable Rocks. Cambridge University Press, New York, NY.

[44] Porter, M.L., Jiménez-Martinez, J., Martinez, R., McCulloch, Q., Carey, J.W., Viswanathan, H.S., 2015. Geo-material microfluidics at reservoir conditions for subsurface energy resource applications. Lab Chip 15, 4044–4053. doi:10.1039/C5LC00704F.

[45] Rahman, M.M., Rahman, M.K., 2010. A review of hydraulic fracture models and development of an improved pseudo-3D model for stimulating tight oil/gas sand. Energy Sources Part A-Recovery Util. Environ. Eff. 32, 1416–1436. doi:10.1080/15567030903060523.

[46] Rassenfoss, S., 2015. What Do Fractures Look Like? A Picture Says A Lot, Even When It is Wrong. J. Petrol. Tech. 67, 60–68. doi:10.2118/0515-0060-JPT.

[47] Roache, P.J., 1998. Verification and Validation in Computational Science and Engineering. Hermosa Publishers, Socorro, New Mexico.

[48] Rosti, M.E., Pramanik, S., Brandt, L., Mitra, D., 2020. The breakdown of Darcy's law in a soft porous material. Soft Matter 16, 939–944. doi:10.1039/C9SM01678C.

[49] Saffman, P.G., 1971. On the boundary condition at the surface of a porous medium. Stud. Appl. Math. 50, 93–101. doi:10.1002/sapm197150293.

[50] Salimzadeh, S., Paluszny, A., Zimmerman, R.W., 2017. Three-dimensional poroelastic effects during hydraulic fracturing in permeable rocks. Int. J. Solids Struct. 108, 153–163. doi:10.1016/j.ijsolstr.2016.12.008.

[51] Sellars, J.R., 1955. Laminar flow in channels with porous walls at high suction Reynolds numbers. J. Appl. Phys. 26, 489–490. doi:10.1063/1.1722024.

[52] Sinton, D., 2014. Energy: the microfluidic frontier. Lab Chip 14, 3127–3134. doi:10.1039/C4LC00267A.

[53] Tavakol, B., Froehlicher, G., Stone, H.A., Holmes, D.P., 2017. Extended lubrication theory: Improved estimates of flow in channels with variable geometry. Proc. R. Soc. A 473, 20170234. doi:10.1098/rspa.2017.0234.

[54] Taylor, G.I., 1971. A model for the boundary condition of a porous material. Part 1. J. Fluid Mech. 49, 319–326. doi:10.1017/S0022112071002088.

[55] Terrill, R.M., Shrestha, G.M., 1964. Laminar flow through parallel and uniformly porous walls of different permeability. Z. Angew. Math. Phys. (ZAMP) 16, 470–482. doi:10.1007/BF01593923.

[56] The OpenFOAM Foundation Ltd, 2020. OpenFOAM. URL: http://www.openfoam.org.

[57] Tian, Z.F., Xu, C., Dowd, P.A., 2018. Numerical simulation of flows in a channel with impermeable and permeable walls using finite volume methods, in: Narayanan, N., Mohanadhas, B., Mangottiri, V. (Eds.), Flow and Transport in Subsurface Environment. Springer, Singapore. Springer Transactions in Civil and Environmental Engineering, pp. 119–140. doi:10.1007/978-981-10-8773-8{_}4.

[58] Tilton, N., Martinand, D., Serre, E., Lueptow, R.M., 2012. Incorporating Darcy's law for pure solvent flow through porous tubes: Asymptotic solution and numerical simulations. AIChE J. 58, 2030–2044. doi:10.1002/aic.13823.

[59] Van Dyke, M., 1987. Slow variations in continuum mechanics. Adv. Appl. Mech. 25, 1–45. doi:10.1016/S0065-2156(08)70276-X.

[60] Vincent, M.C., 2002. Proving It - A Review of 80 Published Field Studies Demonstrating the Importance of Increased Fracture Conductivity, in: Proc. SPE Annual Technical Conference and Exhibition, San Antonio, Texas. doi:10.2118/77675-MS.

[61] Wang, Z., Xu, C., Dowd, P., 2019. Perturbation solutions for flow in a slowly varying fracture and the estimation of its transmissivity. Transp. Porous Med. 128, 97–121. doi:10.1007/s11242-019-01237-7.

[62] Weller, H.G., Tabor, G., Fureby, C., Jasak, H., 1998. A tensorial approach to computational continuum mechanics using object-oriented techniques. Comput. Phys. 12, 620–631. doi:10.1063/1.168744.

[63] Witherspoon, P.A., Wang, J.S.Y., Iwai, K., Gale, J.E., 1980. Validity of Cubic Law for fluid flow in a deformable rock fracture. Water Res. Res. 16, 1016–1024. doi:10.1029/WR016i006p01016.

[64] Yew, C.H., Weng, X., 2015. Mechanics of Hydraulic Fracturing. 2 ed., Gulf Professional Publishing, Waltham, MA. doi:10.1016/C2013-0-12927-3.

[65] Zhang, Q., Prosperetti, A., 2009. Pressure-driven flow in a two-dimensional channel with porous walls. J. Fluid Mech. 631, 1–21. doi:10.1017/S0022112009005837.

[66] Zimmerman, R.W., Bodvarsson, G.S., 1996. Hydraulic conductivity of rock fractures. Transp. Porous Med. 23, 1–30. doi:10.1007/BF00145263.

# Supplementary Material for: The hydraulic conductivity of a shaped fracture with permeable walls*

Daihui Lu[a], Federico Municchi[b] and Ivan C. Christov[a,*,1]

[a]School of Mechanical Engineering, Purdue University, West Lafayette, Indiana 47907, USA
[b]School of Mathematical Sciences, University of Nottingham, University Park, Nottingham, NG7 2RD, UK

ABSTRACT

We investigate the flow-wise variation of the hydraulic conductivity inside a non-uniformly shaped fracture with permeable walls. Using lubrication theory for viscous flows, in conjunction with the Beavers–Joseph–Saffman boundary condition at the permeable walls, we obtain an analytical expression for the velocity profile, conductivity, and wall permeation velocity. These predictions highlight the effects of geometric variation (through the local slope of the aperture's flow-wise variation), the permeability of the walls (through a dimensionless slip coefficient), and the effect of flow inertia (through a Reynolds number). The theory is validated against an OpenFOAM® solver for the Navier–Stokes equations subject to a tensorial slip boundary condition, showing good agreement. The mathematical results have implications on system-level (multiscale) modeling of hydraulically fractured reservoirs, in which the Darcy conductivity of each non-uniform passage must be accurately accounted for, throughout the fractured porous rock.

## Introduction

The supporting material consists of two sections, seven figures S.1 to S.7, and Table S.1.

Supporting Material Section 1 provides the steps in the derivation of the hydraulic conductivity presented and discussed in the main text. These steps are included for completeness and to aid a reader in following the mathematical derivation.

Supporting Material Section 2 describes the OpenFOAM® solver methodology for generating the direct numerical simulation data reported in the main text. Section 2 includes ancillary details about the verification of the simulations (grid independence tests) and post-processing of the simulation data. Toward these ends, Figs. S.1 through S.6 are referenced as part of Section 2.

The OpenFOAM® solver and post-processing scripts are freely available at the repository `https://github.com/daihui-lu/HydraulicConductivityofShapedFractures`, per the "Research data availability" statement in the main text.

Figures S.6 and S.7 are complementary representations of data and information discussed in the main text. They are provided for completeness but are not essential to the conclusions in the main text.

* Acknowledgment is made to the donors of the American Chemical Society Petroleum Research Fund for support of this research under ACS PRF award # 57371-DNI9.

*Corresponding author
christov@purdue.edu ( Ivan C. Christov)
tmnt-lab.org ( Ivan C. Christov)
ORCID(s): 0000-0001-9837-2774 ( Daihui Lu); 0000-0002-5105-6173 ( Federico Municchi); 0000-0001-8531-0531 ( Ivan C. Christov)
[1]Also affiliated with the Center for the Environment at Purdue University.

## 1. Supplementary steps in the main analytical derivations

The Beavers–Joseph–Saffman (BJS) [1, 5] partial slip boundary condition (BC) on the permeable wall is

$$u^* = -\phi\left(\frac{\partial u^*}{\partial z^*} + \epsilon^2\frac{\partial v^*}{\partial x^*}\right) = -\phi\frac{\partial u^*}{\partial z^*} + \mathcal{O}(\epsilon^2) \qquad \text{at} \qquad z^* = \pm h^*(x^*). \tag{S.1}$$

The slip coefficient $\phi$, which is a dimensionless slip length (i.e., $\phi = \ell_{\text{slip}}/h_0$), is an empirically-measurable quantity that enforces a shear stress balance at the porous walls, as discussed in the Introduction of the main text.

Let $\tilde{Re} = \epsilon Re$ be finite as $\epsilon \to 0$. Then, upon taking the limit $\epsilon \to 0$ of Eqs. (2) from the main text, Eq. (2a) remains unchanged, and Eqs. (2b) and (2c) become

$$\tilde{Re}\, u^*\frac{\partial u^*}{\partial x^*} + \tilde{Re}\, v^*\frac{\partial u^*}{\partial z^*} = -\frac{\partial p^*}{\partial x^*} + \frac{\partial^2 u^*}{\partial z^{*2}}, \tag{S.2a}$$

$$0 = -\frac{\partial p^*}{\partial z^*}. \tag{S.2b}$$

Now, assume a regular perturbation expansion in $\tilde{Re} \ll 1$. The velocity field is expanded as

$$u^* = u_0^* + \tilde{Re}\, u_1^* + \cdots, \tag{S.3a}$$

$$v^* = v_0^* + \tilde{Re}\, v_1^* + \cdots. \tag{S.3b}$$

Substituting Eqs. (S.3) into Eqs. (S.2) and neglecting $\mathcal{O}(\tilde{Re})$ and higher-order terms, we obtain the leading-order momentum equations:

$$0 = -\frac{\partial p^*}{\partial x^*} + \frac{\partial^2 u_0^*}{\partial z^{*2}}, \tag{S.4a}$$

$$0 = -\frac{\partial p^*}{\partial z^*}, \tag{S.4b}$$

subject to the boundary conditions (BCs):

$$\underbrace{\left.\frac{\partial u_0^*}{\partial z^*}\right|_{z^*=0} = 0, \quad \left.v_0^*\right|_{z^*=0} = 0}_{\text{symmetry}} \quad \text{and} \quad \underbrace{\left.u_0^*\right|_{z^*=h^*} = -\,\phi\left.\frac{\partial u^*}{\partial z^*}\right|_{z^*=h^*}}_{\text{BJS BC}}. \tag{S.5}$$

Recall that, by symmetry, we are only solving for the profile in the top half of the fracture. Therefore, the leading-order solution for the horizontal velocity has the form

$$u_0^*(x^*, z^*) = \frac{1}{2}\frac{dp^*}{dx^*}z^{*2} + \mathfrak{C}_1(x^*)z^* + \mathfrak{C}_2(x^*), \tag{S.6}$$

where $\mathfrak{C}_1$ and $\mathfrak{C}_2$ are arbitrary (integration) functions of $x^*$. Since $p^*$ is independent of $z^*$ by Eq. (S.4b), henceforth we write $\partial p^*/\partial x^* = dp^*/dx^*$. Imposing the boundary conditions (S.5) onto Eq. (S.6), we obtain

$$u_0^*(x^*, z^*) = \left(\frac{h^{*2} - z^{*2}}{2} + \phi h^*\right)\left(-\frac{dp^*}{dx^*}\right). \tag{S.7}$$

Since the flow is in the direction of positive $x^*$, $dp^*/dx^* < 0$, so we choose to associate a negative sign with this term in some equations, for clarity, as is standard in the fluid mechanics literature. Then, the leading-order depth-averaged velocity is

$$\langle u_0^*\rangle(x^*) = \frac{1}{h^*(x^*)}\int_0^{h^*(x^*)} u_0^*(x^*, z^*)\, dz^* = \frac{3\phi h^*(x^*) + h^*(x^*)^2}{3}\left(-\frac{dp^*}{dx^*}\right). \tag{S.8}$$

Next, we determine the leading-order vertical velocity. From the conservation of mass equation,

$$\frac{\partial u^*}{\partial x^*} + \frac{\partial v^*}{\partial z^*} = 0, \tag{S.9}$$

we deduce that

$$\frac{\partial v_0^*}{\partial z^*} = -\frac{\partial u_0^*}{\partial x^*} = \left(h^* \frac{dh^*}{dx} + \phi \frac{dh^*}{dx}\right) \frac{dp^*}{dx^*} - \left(\frac{z^{*2} - h^{*2}}{2} - \phi h^*\right) \frac{d^2 p^*}{dx^{*2}}. \tag{S.10}$$

Now, integrating both sides of Eq. (S.10) from 0 to an arbitrary $z^*$, and using the second boundary condition in Eq. (S.5), we find that the vertical velocity is

$$v_0^*(x^*, z^*) = \left(h^* \frac{dh^*}{dx} + \phi \frac{dh^*}{dx}\right) z^* \frac{dp^*}{dx^*} - \left(\frac{z^{*3}}{6} - \frac{h^{*2} z^*}{2} - \phi h^* z^*\right) \frac{d^2 p^*}{dx^{*2}}. \tag{S.11}$$

From Eqs. (S.2), we obtain the first-order perturbation equation:

$$u_0^* \frac{\partial u_0^*}{\partial x^*} + v_0^* \frac{\partial u_0^*}{\partial z^*} = \frac{\partial^2 u_1^*}{\partial z^{*2}}. \tag{S.12}$$

Substituting the $\mathcal{O}(1)$ solution from Eq. (S.7) above into Eq. (S.12), we obtain

$$\frac{\partial^2 u_1^*}{\partial z^{*2}} = \left[\left(\frac{h^{*2}}{2} + \phi h^*\right)^2 + \frac{z^{*4}}{12}\right] \frac{dp^*}{dx^*} \frac{d^2 p^*}{dx^{*2}} + \left(\frac{h^{*2} + z^{*2}}{2} + \phi h^*\right)(h^* + \phi) \frac{\alpha}{\epsilon} \left(\frac{dp^*}{dx^*}\right)^2, \tag{S.13}$$

subject to homogeneous BCs:

$$\left.\frac{\partial u_1^*}{\partial z^*}\right|_{z^*=0} = 0 \quad \text{and} \quad \left.u_1^*\right|_{z^*=h^*} = 0. \tag{S.14}$$

Integrating both sides of Eq. (S.13) from 0 to an arbitrary $z^*$, and substituting the boundary conditions from Eq. (S.14), we obtain the first-order inertial correction to the horizontal velocity component:

$$\begin{aligned} u_1^*(x^*, y^*) = &\left[\left(\frac{h^{*2}}{2} + \phi h^*\right)^2 \frac{z^{*2} - h^{*2}}{2} + \frac{1}{360}\left(z^{*6} - h^{*6}\right)\right] \frac{dp^*}{dx^*} \frac{d^2 p^*}{dx^{*2}} \\ &+ \left[\left(\frac{h^{*2}}{2} + \phi h^*\right) \frac{z^{*2} - h^{*2}}{2} + \frac{z^{*4} - h^{*4}}{24}\right](h^* + \phi) \frac{\alpha}{\epsilon} \left(\frac{dp^*}{dx^*}\right)^2. \end{aligned} \tag{S.15}$$

From the latter, we find the depth-averaged velocity correction:

$$\begin{aligned} \langle u_1^* \rangle &= \frac{1}{h^*(x^*)} \int_0^{h^*(x^*)} u_1^*(x^*, z^*)\, dz^* \\ &= \left(\frac{3}{35} h^{*6} + \frac{1}{3}\phi h^{*5} + \frac{\phi^2}{3} h^{*4}\right)\left(-\frac{dp^*}{dx^*}\right) \frac{d^2 p^*}{dx^{*2}} - \left(\frac{1}{5} h^{*4} + \frac{1}{3}\phi h^{*3}\right)(h^* + \phi) \frac{\alpha}{\epsilon} \left(\frac{dp^*}{dx^*}\right)^2. \end{aligned} \tag{S.16}$$

To close the problem, we need another constraint. Mohais et al. [3] provided one solution by assuming a *constant* permeation velocity $v_w$ in a parallel fracture ($\alpha = 0$, $h^* = 1$), i.e., $v_0\big|_{z=\pm h} = \pm v_w$ ($v_0^*\big|_{z^*=\pm 1} = \pm 1$). If we apply this constraint to the above analysis, the dimensionless average horizontal velocity becomes

$$\begin{aligned} \langle u^* \rangle &= \left[\frac{3\phi + 1}{3} + \tilde{Re}\left(\frac{3}{35} + \frac{1}{3}\phi + \frac{\phi^2}{3}\right) \frac{3}{3\phi + 1}\right]\left(-\frac{dp^*}{dx^*}\right) \\ &= \left(\frac{3\phi + 1}{3}\right)\left[1 + \tilde{Re}\left(\frac{3}{35} + \frac{1}{3}\phi + \frac{\phi^2}{3}\right) \frac{9}{(3\phi + 1)^2}\right]\left(-\frac{dp^*}{dx^*}\right). \end{aligned} \tag{S.17}$$

This solution differs from [3] in that the we have expanded only the velocity $u^*$ in powers of $\tilde{Re}$, while Mohais et al. [3] expanded $p^*$ as well and obtained (using our notation):

$$-\frac{dp^*}{dx^*} = \langle u^* \rangle \left\{\frac{3}{1 + 3\phi} - \tilde{Re}\left[\frac{9(7\phi + 1)}{140(1 + 3\phi)^3} + \left(\frac{3 + 6\phi}{2 + 6\phi}\right)^2\right]\right\}. \tag{S.18}$$

To the leading order in $\tilde{Re}$, we may use the Taylor series $(1-\xi)^{-1} = 1 + \xi + \mathcal{O}(\xi^2)$ to rewrite (S.18) as

$$\langle u^* \rangle = \left( \frac{3\phi + 1}{3} \right) \left\{ 1 + \tilde{Re} \left[ \frac{3(7\phi + 1)}{140(3\phi + 1)^2} + \frac{3(2\phi + 1)^2}{4(3\phi + 1)} \right] \right\} \left( -\frac{dp^*}{dx^*} \right). \tag{S.19}$$

Despite the different expansion methods used to obtain Eqs. (S.17) and (S.19), the leading-order terms are the same, i.e., they both yield:

$$\langle u^* \rangle = \frac{1}{3}(1 + 3\phi) \left( 1 + \frac{27}{35}\tilde{Re} \right) \left( -\frac{dp^*}{dx^*} \right) + \mathcal{O}(\tilde{Re}^2, \phi^2, \phi\tilde{Re}), \tag{S.20}$$

meaning they are asymptotically equivalent for $\phi \ll 1$ and $\tilde{Re} \ll 1$.

Now, however, the wall permeation velocity $v_w$ (and its relation to the pressure gradient $dp/dx$) is not necessarily known *a priori*. To close the problem, we apply the flux constraint $\langle u_0^* \rangle = 1$ to Eq. (S.8), and we obtain

$$\frac{dp^*}{dx^*} = -\frac{3}{3\phi h^*(x^*) + h^*(x^*)^2} \qquad \Rightarrow \qquad \frac{d^2p^*}{dx^{*2}} = \frac{(9\phi + 6h^*)\delta}{[3\phi h^*(x^*) + h^*(x^*)^2]^2}. \tag{S.21}$$

Substituting the latter results into Eq. (S.16) and suppressing the explicit notation that $h^*$ is a function of $x^*$, we have

$$\langle u_1^* \rangle = \frac{h^{*3}(28\phi^{*2} + 22\phi h^* + 3h^{*2})\delta}{35(3\phi + h^*)^2} \frac{dp^*}{dx^*}. \tag{S.22}$$

Finally, from Eqs. (S.8) and (S.22), $\langle u^* \rangle$ can be reconstituted into a Darcy's law, as shown in Eq. (8) in the main text and discussed therein.

## 2. Implementation of the numerical solver and its verification

The solution algorithm for the incompressible Navier–Stokes equations [Eqs. (2) in the main text] used in our direct numerical simulation (DNS) study is SIMPLE (*semi-implicit method for pressure-linked equations*) [see, e.g., 4, Ch. 15]. In this study, we set the tolerance for the pressure and velocity components' residuals to be $10^{-5}$ (see the example convergence plot in Fig. S.1). The BCs applied in the simulation are summarized in the schematic in Fig. S.2. In particular, note that the BJS BC (S.1) is, mathematically, a Robin (or mixed-type) BC. However, within the iterative algorithm, we reformulated it as a Dirichlet boundary condition to enhance stability and ensure consistency of fluxes within the pressure iterations.

The BJS BC, as given in the computational paper by Layton et al. [2], is essentially a slip condition enforcing a specific value of the velocity field in the face-planar direction of the boundary cell. In this formulation, the condition does not alter the velocity normal to the porous walls.

In OpenFOAM® [7, 6] and, more generally, in the finite volume method [4], discretization is performed by summing all the contribution from the volumetric source terms (if present) and fluxes, looping over all the cell faces. In order to discretize generic differential equations without any specific knowledge of the form of the fluxes, OpenFOAM® requires that each flux is expressed in terms of a face value $\boldsymbol{u}_f$ and a face-normal gradient $(\nabla \boldsymbol{u})_f \cdot \boldsymbol{n}_f$, where $f$ is a generic face and $\boldsymbol{n}_f$ is the vector normal to such face. Therefore, an explicit or implicit (i.e., matrix coefficients) expression for those two face-based fields is required. Boundary faces are no exception. Thus, with reference to Fig. S.3, it is necessary to provide expressions for $\boldsymbol{u}_b$ and $(\nabla \boldsymbol{u})_b \cdot \boldsymbol{n}$ that take into account the BJS BC. In vector form,

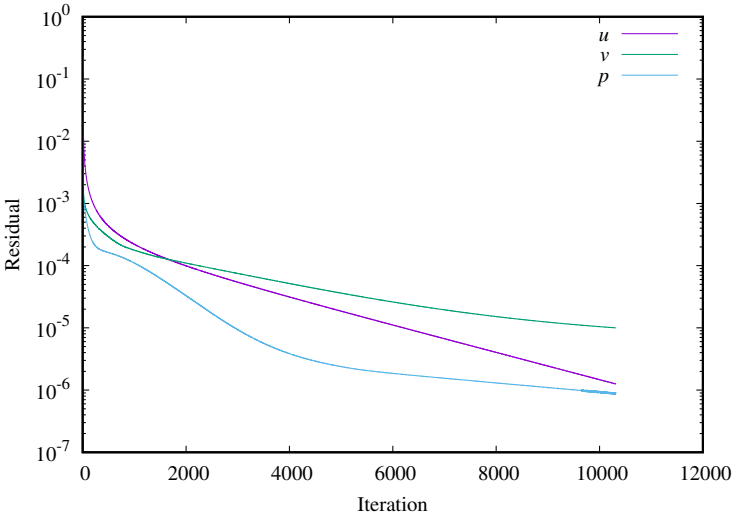


**Figure S.1:** SIMPLE algorithm's residuals plot for a sample simulation with $\alpha = -10^{-3}$, $\phi = 5 \times 10^{-4}$ and $\tilde{Re} = 0.01$. The tolerance used is $10^{-5}$ for both the pressure residual and each velocity component's residual. The simulation converges after about 10 000 iterations.

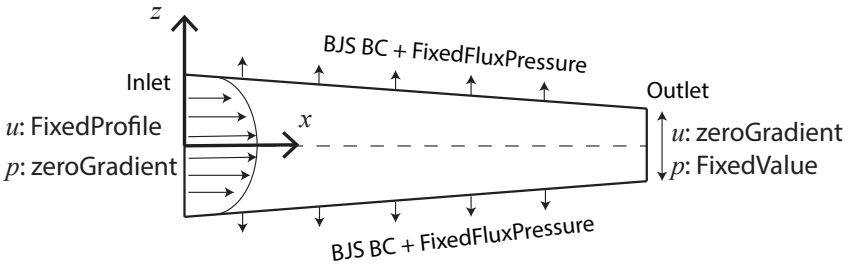


**Figure S.2:** Schematic of the OpenFOAM® boundary conditions used in the numerical simulations.

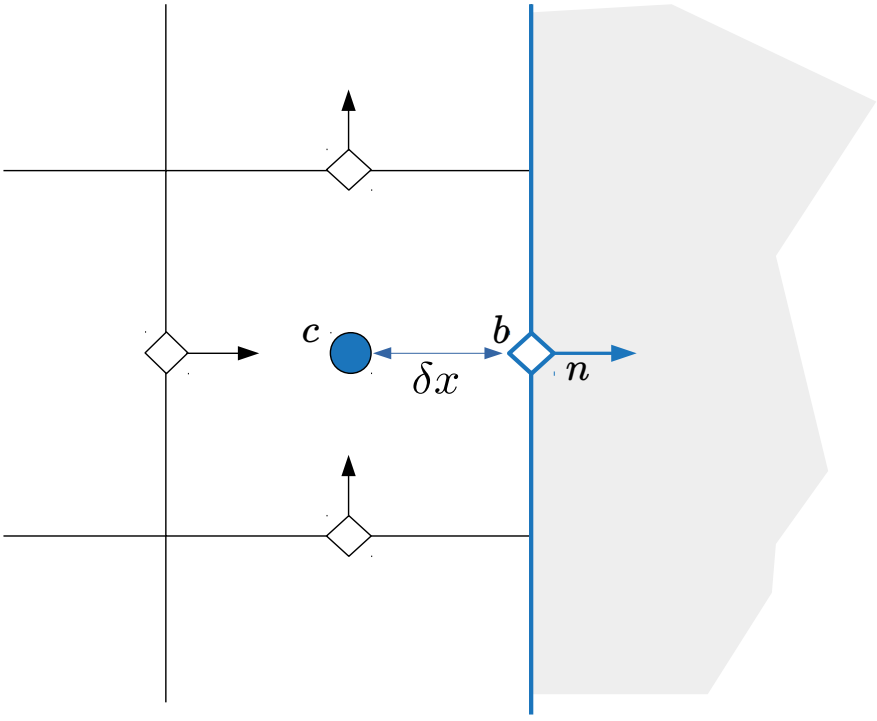


**Figure S.3:** Illustration of a boundary cell with face centers an face normals. In this figure, $c$ is the cell center (blue dot) and the blue line represents the boundary. The BJS BC is applied at point $b$, corresponding to the center of the boundary face, where $\delta x$ is the distance between $b$ and $c$, and $\boldsymbol{n}$ is the vector normal to the boundary face.

the boundary condition reads:

$$\mathbf{T} \cdot \boldsymbol{u}_b = -\mathbf{T} \cdot \left( \ell \frac{\partial \boldsymbol{u}}{\partial n} \right)_b , \tag{S.23}$$

where $\mathbf{T} = (\mathbf{I} - \boldsymbol{nn})$ is the projector on the tangential plane, $\mathbf{I}$ is the identity operator, and $\ell = \ell_{\text{slip}}$ is the BJS slip length discussed in the main text.

However, a problem described by the Navier–Stokes equations with a BC of the type in Eq. (S.23) is not well posed, since such condition only constrains the face-planar field. Therefore, it is necessary to specify a condition on the face-normal field. Since the BJS BC does not provide such a constrain, we assume that all the flow arriving normal to the boundary leaves the domain. This assumption corresponds to:

$$\boldsymbol{n} \cdot \left( \frac{\partial \boldsymbol{u}}{\partial n} \right)_b = 0 . \tag{S.24}$$

In this sense, condition (S.24) merely correspond to copying the value of the velocity field in the first cell. In fact, using a linear interpolation scheme one obtains:

$$\boldsymbol{n} \cdot \left( \frac{\partial \boldsymbol{u}}{\partial n} \right)_b \approx \frac{\boldsymbol{n} \cdot (\boldsymbol{u}_b - \boldsymbol{u}_c)}{\delta x} , \tag{S.25}$$

which results in:

$$\boldsymbol{n} \cdot \boldsymbol{u}_b = \boldsymbol{n} \cdot \boldsymbol{u}_c . \tag{S.26}$$

Equation (S.23) is also discretized using a linear interpolation scheme:

$$\mathbf{T} \cdot \boldsymbol{u}_b = -\mathbf{T} \cdot \left( \ell \frac{\boldsymbol{u}_b - \boldsymbol{u}_c}{\delta x} \right) = \mathbf{T} \cdot \left( \ell \frac{\boldsymbol{u}_c}{\delta x + \ell} \right) . \tag{S.27}$$

The final form of the BC is then implemented as a Dirichlet BC:

$$\boldsymbol{u}_b = \boldsymbol{n}(\boldsymbol{n}\cdot\boldsymbol{u}_b) + \mathbf{T}\cdot\boldsymbol{u}_b = \boldsymbol{n}(\boldsymbol{n}\cdot\boldsymbol{u}_b) + \mathbf{T}\cdot\left(\ell\frac{\boldsymbol{u}_c}{\delta x+\ell}\right). \tag{S.28}$$

This formulation clearly requires multiple fixed point iterations that, if they converge, result in the correct calculation of $\boldsymbol{u}_p$ up to second-order accuracy. For the pressure field, we employ a *fixedFluxPressure* BC, which essentially imposes a pressure gradient based on the flux leaving the domain, and allows the simulation to self-consistently determine the wall permeation velocity.

Since we study steady flow, the initial conditions are only relevant for the convergence (rather than the accuracy), so they are simply specified as zero velocity and zero pressure. At the inlet of the fracture ($x = 0$), we impose the theoretically computed velocity profile given by Eqs. (S.7) and (S.10) (with $dp^*/dx^*$ computed from Eq. (S.16) under the constraint $\langle u^*\rangle = 1$), which has a non-zero permeation velocity and satisfies the BJS BC at the inlet's walls ($z = \pm h_0$). A zero-gradient velocity BC is employed across the outlet plane ($x = L$), and the pressure there is set to zero gauge pressure (see Fig. S.2). We do not consider the case of a closed fracture, so we do not need to impose a crack-tip condition.

To find the optimal computational grid arrangement for the simulations results presented in the main text, we ran a series of test cases with different numbers of grid elements and with different grid resolutions (spacing), as summarized in Table S.1. The simulations can be considered non-dimensional (the fluid's physical properties are chosen to fix the dimensionless parameters such as $\tilde{Re}$). To maintain $\epsilon$, the simulation channel has length $L = 100$ and inlet half-aperture $h_0 = 1$. From each simulation, we extracted the velocities at the cross-sectional plane located at $x = L/2$ ($x^* = 0.5$). We also extracted the pressure gradient $dp/dx$ variation along the whole channel. Then, we calculated the percent change of these quantities with respect to the theoretical values (see above). Finally, the velocities from the simulations were rescaled by $\langle u\rangle$ to be comparable to the theory, since the constraint $\langle u\rangle = 1$ was imposed in the derivation.

The grid independence study revealed that the optimal choice is 4000 grid elements with $\Delta x = 0.5$ and $\Delta z = 0.05$, as it showed significantly better performance on the permeation velocity than coarser girds and finer grids did not improve the accuracy notably (see Fig. S.4). The slip velocity and axial pressure gradient showed convergence for 4000 grid elements, with the error increasing for larger grids. Therefore, we used 4000 grid elements for all DNS results reported in the main text. Note that a non-uniform grid spacing (see Fig. S.5) was used in the vertical direction to better resolve the flow near the porous walls.

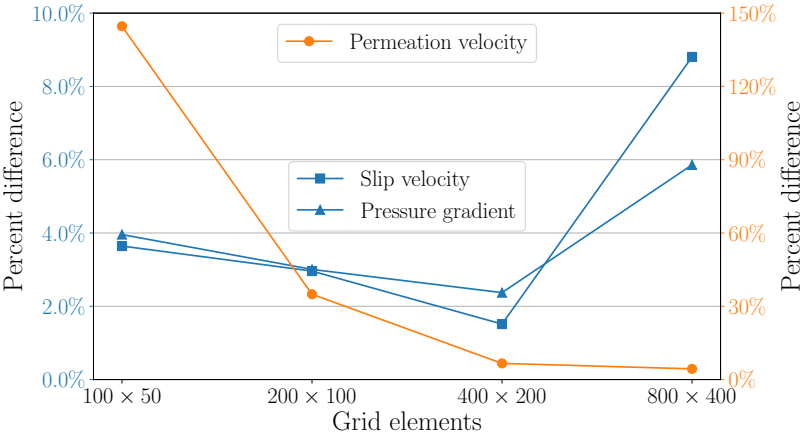


**Figure S.4:** Grid independence of key (dimensionless) flow quantities. Percent difference (relative to the theoretical solution in the main text) of the wall permeation velocity $v^*\big(x^*, h^*(x^*)\big)$, the wall slip velocity $u^*\big(x^*, h^*(x^*)\big)$, and the axial component of the pressure gradient $dp^*/dx^*$, all evaluated at $x^* = 0.5$ but using different grids.

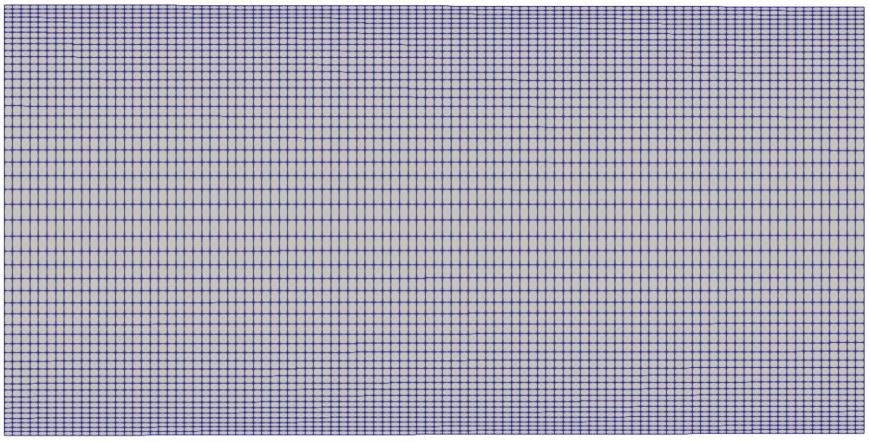

**Figure S.5:** Schematic of the computational grid showing the non-uniform vertical spacing ("boundary layer meshing"). Notice that the grid spacing is scaled in the horizontal direction to fit the figure.

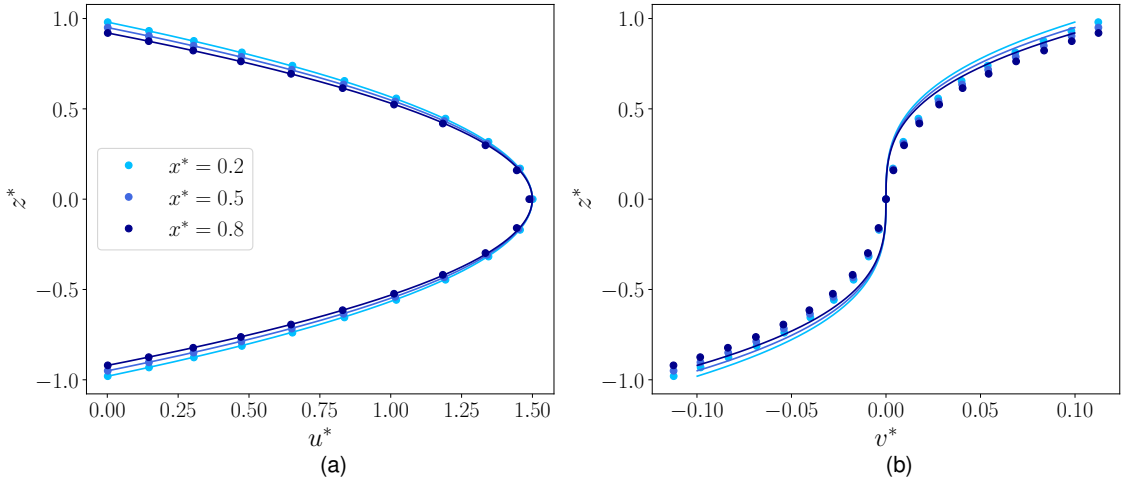


**Figure S.6:** Flow-wise variation: Dimensionless velocity profiles versus fracture aperture $z^*$ at the planes $x^* \in \{0.2, 0.5, 0.8\}$, for $\alpha = -10^{-3}$, $\phi = 10^{-4}$ and $\tilde{Re} = 0.01$: (a) the horizontal component $u^*(x^*, z^*)$; (b) the vertical component $v^*(x^*, z^*)$. Solid curves are the theoretical profiles from Eq. (S.11), and filled circles with the same colors are the corresponding simulation results. Profiles are color-coded by their $x^*$ positions.

**Table S.1**
Information about the grids used to establish grid independence of the direct numerical simulation results.

| Grid arrangement | $100 \times 50$ | $200 \times 100$ | $400 \times 200$ | $800 \times 400$ |
|---|---|---|---|---|
| Total grid elements | 5 000 | 20 000 | 80 000 | 320 000 |
| $\Delta x$ resolution | 1 | 0.5 | 0.25 | 0.125 |
| $\Delta z$ resolution | 0.02 | 0.01 | 0.005 | 0.0025 |

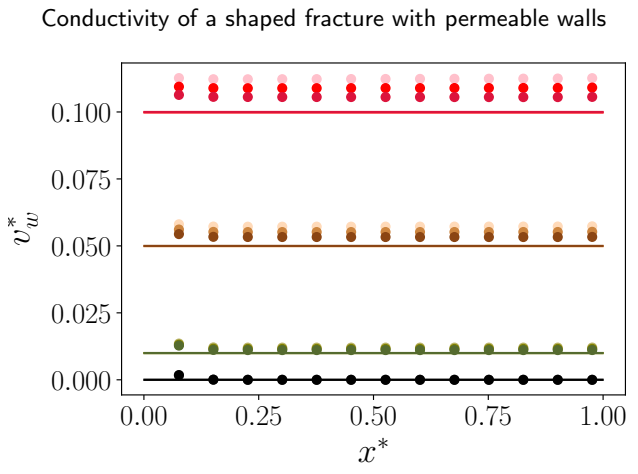


**Figure S.7:** The dimensionless wall permeation velocity $v_w^*(x^*)$ along the channel for $\tilde{Re} = 0.01$. Colors represent cases with different $\alpha$ and $\phi$ values: ●●●: $\alpha = 0$, $\phi \in \{0, 5 \times 10^{-4}, 10^{-3}\}$; ●●●: $\alpha = -10^{-4}$, $\phi \in \{0, 5 \times 10^{-4}, 10^{-3}\}$; ●●●: $\alpha = -5 \times 10^{-3}$, $\phi \in \{0, 5 \times 10^{-4}, 10^{-3}\}$; ●●●: $\alpha = -10^{-3}$, $\phi \in \{0, 5 \times 10^{-4}, 10^{-3}\}$. Filled circles represent the simulation results, and solid curves of the same color represent the corresponding theoretical predictions.

## References


[1] Beavers, G.S., Joseph, D.D., 1967. Boundary conditions at a naturally permeable wall. J. Fluid Mech. 30, 197–207. doi:10.1017/S0022112067001375.

[2] Layton, W.J., Schieweck, F., Yotov, I., 2002. Coupling fluid flow with porous media flow. SIAM J. Numer. Anal. 40, 2195–2218. doi:10.1137/S0036142901392766.

[3] Mohais, R., Xu, C., Dowd, P.A., Hand, M., 2012. Permeability correction factor for fractures with permeable walls. Geophys. Res. Lett. 39, L03403. doi:10.1029/2011GL050519.

[4] Moukalled, F., Mangani, L., Darwish, M., 2016. The Finite Volume Method in Computational Fluid Dynamics: An Advanced Introduction with OpenFOAM® and Matlab. Fluid Mechanics and its Applications, Springer International Publishing, Cham, Switzerland. doi:10.1007/978-3-319-16874-6.

[5] Saffman, P.G., 1971. On the boundary condition at the surface of a porous medium. Stud. Appl. Math. 50, 93–101. doi:10.1002/sapm197150293.

[6] The OpenFOAM Foundation Ltd, 2020. OpenFOAM. URL: http://www.openfoam.org.

[7] Weller, H.G., Tabor, G., Fureby, C., Jasak, H., 1998. A tensorial approach to computational continuum mechanics using object-oriented techniques. Comput. Phys. 12, 620–631. doi:10.1063/1.168744.